The current issue and full text archive of this journal is available on Emerald Insight at:
https://www.emerald.com/insight/0332-1649.htm



Received 19 September 2021
Revised 1 February 2022
16 March 2022
Accepted 17 March 2022

# Proposing a sequential iterative method based on a per-unit model for rotor shape optimization in permanent magnet assisted synchronous reluctance motors

Ali Jamali Fard and Mojtaba Mirsalim
*Department of Electrical Engineering, Electrical Machines and Transformer Research Laboratory (EMTRL), Amirkabir University of Technology, Tehran, Iran*

## Abstract

**Purpose** – During the design process of synchronous reluctance motors (SynRMs), one crucial step, after its main dimensioning, is optimizing the rotor geometry for maximum average torque and minimum torque ripple. However, because of the complexity of rotor flux-barrier layers geometry, the number of rotor geometrical parameters is high and this step could be quite complex and time-consuming. To obtain a good performance, one needs a robust algorithm to optimize the rotor geometry. The purpose of this paper is to present a sequential iterative method for rotor shape optimization in SynRMs based on the per-unit rotor model to maximize the average torque and minimize the torque ripple.

**Design/methodology/approach** – In the presented method, at first, rotor geometrical parameters are classified into several groups based on their geometrical similarities, and then optimization is done on these individual groups iteratively. The method starts with an arbitrary feasible rotor geometry and proceeds to optimize it. Because the method's performance depends on initial rotor geometry, different cases are studied to investigate the convergence and robustness of the method. The MATLAB software is used to implement the optimization algorithm, and the ANSYS Maxwell software is used for the finite element analysis.

**Findings** – The performance of the proposed method is studied on a three-phase 0.75 kW-1,500 rpm permanent magnet assisted SynRM. The results show that the method improves the average torque while reducing the torque ripple. Even if the method starts with an inappropriate initial rotor geometry, it is robust enough and converges within an acceptable number of iterations.

**Originality/value** – The value of this paper is in introducing a per-unit rotor model. When the authors optimize the rotor geometry for a specific motor rating, it can be scaled up or down for other ratings with little effort. In this work, the number of rotor poles is four and the number of rotor flux-barrier layers per pole is three. Other combinations could be analyzed in future studies.

**Keywords** Synchronous reluctance motors (SynRMs), Permanent magnet assisted SynRMs (PMaSynRMs), Rotor shape optimization, Finite element analysis (FEA), Electrical machines, Shape optimization, Permanent magnet machine

**Paper type** Research paper

COMPEL - The international journal for computation and mathematics in electrical and electronic engineering
Vol. 41 No. 5, 2022
pp. 1826-1848
© Emerald Publishing Limited
0332-1649
DOI 10.1108/COMPEL-09-2021-0340

## 1. Introduction

Synchronous reluctance motors (SynRMs) are a viable alternative to induction motors (IMs) in variable speed inverter-driven applications (Baka *et al.*, 2021; Cai *et al.*, 2014; Cupertino *et al.*, 2014). They are used in applications in which synchronous speed, high dynamics, wide flux weakening region and fault-tolerant capability are needed (Bacco and Bianchi, 2019;

Bianchi *et al.*, 2008; Guan *et al.*, 2016). High dynamic performance is achievable thanks to several air flux-barrier layers because of the low rotor moment-of-inertia. SynRM is fault-tolerant because there is no excitation on the rotor, and in the case of the stator winding short circuits, there will be no induced back-emf. The torque density of SynRM is higher than IM, and therefore, it allows size reduction for the same rating (Cupertino *et al.*, 2014); López-Torres *et al.*, 2018). In addition, for the same output power and motor size, SynRM can reach a higher efficiency class compared to IM (Liu *et al.*, 2019; Mingardi and Bianchi, 2017).

The stator core design of SynRM is like the IM, whereas the rotor geometry is different. The developed torque in this motor is of reluctance type, and it is proportional to the rotor magnetic saliency ratio. A drawback of SynRM is its power factor. The volt-ampere rating of the inverter of a SynRM is commonly 20%–30% higher than the motor output power (Pellegrino *et al.*, 2016; Wang *et al.*, 2015). The power factor is a function of the saliency ratio. Therefore, a high value for saliency ratio is desirable to get a good performance.

Several methods are presented in the literature for rotor shape optimization of SynRMs. A procedure for the automatic design of multi-layer SynRMs based on finite element analysis (FEA) and multi-objective optimization algorithms is presented in Cupertino *et al.* (2014). Choi *et al.* (2008) implement the response surface method, and the optimal design is found by comparing inductance difference and torque ripple, considering the desired operating objectives. An analytical model is developed by Bianchi *et al.* (2008), showing the dependence of the torque ripple on the rotor geometry. In the developed model, the interaction of the electric loading harmonics and the rotor geometry on the torque was investigated, and the position of the flux-barrier ends was chosen to minimize one or more torque harmonics of a given order. To further reduce torque ripple, two different types of laminations were combined to compensate for other torque harmonics. In this paper, flux-barrier ends are circular arcs and the diameter of these arcs are decision variables in the optimization.

Because of the existence of a high number of blank spaces in the rotor lamination of SynRMs, we should pay particular attention to validating the mechanical robustness of the rotor for high torque and high-speed applications Babetto *et al.* (2018), Tarek and Choi (2017). A study on rotor shape optimization in SynRMs considering mechanical stress analysis of the rotor under high-speed operation was presented by Tarek and Choi (2017). It was mentioned that adding mini flux-barrier layers in each of the rotor flux-barrier layers can reduce stress significantly. In this paper, two radial ribs were considered in each rotor flux-barriers.

There are several advantages when permanent magnets (PMs) are inset within the rotor flux–barrier layers. A part of the PM flux tends to saturate the iron bridges in the rotor. Such a saturation implies a beneficial reduction of Lq (Liu *et al.*, 2016; Pellegrino *et al.*, 2016). Moreover, the PMs added along the negative $q$-axis compensate for the negative flux, and as a result, an alignment electromagnetic torque is added to the reluctance torque term. This study presents a robust rotor shape optimization method for three-phase PM assisted SynRMs (PMaSynRM).

## 2. Rotor per-unit model

Figure 1(a) shows the rotor geometry. In this figure, $D_{sh}$ is the shaft diameter, $D$ is the stator bore diameter and $g$ is the air-gap length. There are three flux-barrier layers per pole. Implementing three flux-barriers results in a higher and smoother torque Babetto *et al.* (2018). Every flux-barrier layer has a rectangle shape geometry in its middle to allow cubic magnet insertion. Flux-barrier layers end with a circular arc to avoid local electromagnetic hot points at the rotor surface. There are two radial ribs in each flux-barrier layer to confirm the mechanical robustness of the rotor at high speeds.

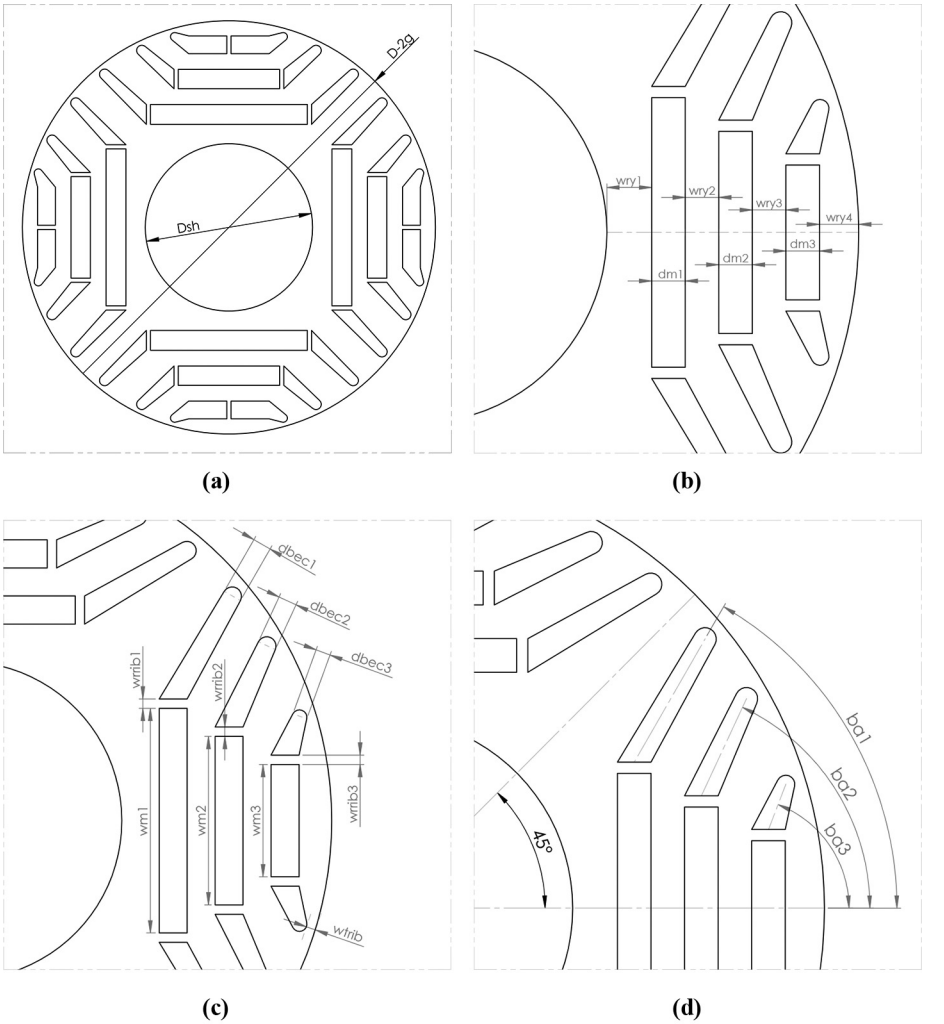


**Figure 1.**
Geometrical parameters of the rotor lamination

**Notes:** (a) Geometry of rotor lamination; (b) width of rotor yokes, depth of magnets; (c) width of magnets, width of ribs, diameter of barrier end circles; (d) barrier angles

*2.1 Decision variables*

Rotor geometrical parameters are as follows:

- Width of rotor iron yokes or flux-carrier layers [shown in Figure 1(b)],

$$\{wry_1, wry_2, wry_3, wry_4\} \tag{1}$$

Total width of the rotor iron yoke,

$$wry = wry_1 + wry_2 + wry_3 + wry_4 \tag{2}$$

- Depth of magnets [shown in Figure 1(b)],

$$\{dm_1, dm_2, dm_3\} \tag{3}$$

- Width of magnets [shown in Figure 1(c)],

$$\{wm_1, wm_2, wm_3\} \tag{4}$$

- Diameter of barrier end circles [shown in Figure 1(c)],

$$\{dbec_1, dbec_2, dbec_3\} \tag{5}$$

- Width of tangential rib [shown in Figure 1(c)],

$$\{wtrib\} \tag{6}$$

- Width of radial ribs [shown in Figure 1(c)],

$$\{wrrib_1, wrrib_2, wrrib_3\} \tag{7}$$

- Barrier angles [shown in Figure 1(d)],

$$\{ba_1, ba_2, ba_3\} \tag{8}$$

- Shaft diameter or air factor (air insulation ratio),

$$\{D_{\text{sh}} \text{ or } K_{\text{air}}\} \tag{9}$$

The rotor air insulation ratio or air factor $K_{\text{air}}$ is defined as follows:

$$K_{\text{air}} = \frac{\sum_{i=1}^{3} dm_i}{\sum_{i=1}^{4} wry_i + \sum_{i=1}^{3} dm_i} = \frac{\sum_{i=1}^{3} dm_i}{wry + \sum_{i=1}^{3} dm_i} \tag{10}$$

The shaft diameter and air insulation ratio are related to each other via the following equation:

$$\frac{wry}{1 - K_{\text{air}}} = \frac{D}{2} - g - \frac{D_{\text{sh}}}{2} \tag{11}$$

Among these two variables, one of them can be selected as a decision variable during the optimization. In the developed algorithm in this paper, $D_{\text{sh}}$ is considered as a dependent variable and $K_{\text{air}}$ is a decision optimization variable.

*2.2 Per-unit variables*

Figure 2 illustrates the flux lines due to balanced excitation of the stator winding while there is no flux-barrier layer inside the rotor. The flux lines pattern for solid rotor structure could be used as an indication of the optimal rotor geometry. According to the flux lines pattern for the solid rotor, we can conclude the following inequalities:

$$\begin{cases} wry_2 \leq wry_1 \\ wry_3 \leq wry_2 \\ wry_4 \leq wry_3 \end{cases} \tag{12}$$

$$\begin{cases} dm_2 \leq dm_1 \\ dm_3 \leq dm_2 \end{cases} \tag{13}$$

$$2\left(\frac{D_{\text{sh}}}{2} + wry_1\right)\tan\left(\frac{\alpha_p}{2}\right) \geq wm_1 \geq wm_2 \geq wm_3 \tag{14}$$

$$ba_3 \geq ba_2 \geq ba_1 \geq \frac{\pi}{p} \tag{15}$$

($p$ in equation (15) is the number of rotor poles)

$$\begin{cases} dbec_1 \leq dm_1 \times \sin(ba_1) \\ dbec_2 \leq dm_2 \times \sin(ba_2) \\ dbec_3 \leq dm_3 \times \sin(ba_3) \end{cases} \tag{16}$$

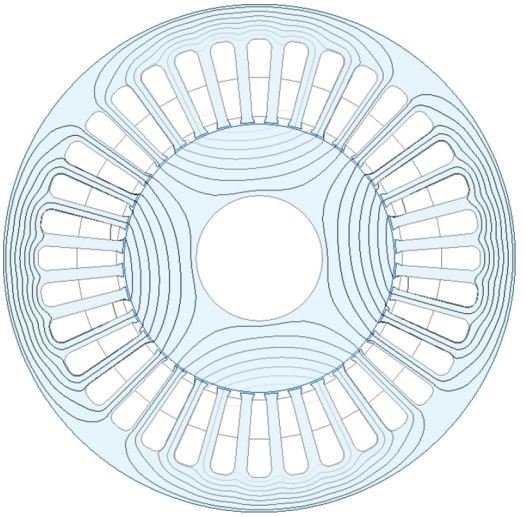

**Figure 2.**
Flux lines due to balanced excitation of the stator winding for the solid rotor structure

The constraints mentioned in equation (12) can be translated into another form if we define the following unitless variables:

$$\begin{cases} \gamma_{wry2} = \dfrac{wry_2}{wry_1} \leq 1 \\ \gamma_{wry3} = \dfrac{wry_3}{wry_2} \leq 1 \\ \gamma_{wry4} = \dfrac{wry_4}{wry_3} \leq 1 \end{cases} \tag{17}$$

Considering the defined variables introduced in equation (17), instead of working with the following collection:

$$\{wry_1, wry_2, wry_3, wry_4\} \tag{18}$$

The new collection introduced in equation (19) will be used:

$$\{wry,\ \gamma_{wry2} \leq 1,\ \gamma_{wry3} \leq 1,\ \gamma_{wry4} \leq 1\} \tag{19}$$

However, in this case, a proper indication of the value of per-unit variables exists. The first variable in this list is the total width of rotor yokes. The initial value for *wry* is calculated based on half of the pole flux and the assumed maximum flux density in the rotor yokes during the main dimensioning step.

A similar procedure is used for defining other variable groups. For the depth of magnets, we can define:

$$\begin{cases} \gamma_{dm2} = \dfrac{dm_2}{dm_1} \leq 1 \\ \gamma_{dm3} = \dfrac{dm_3}{dm_2} \leq 1 \end{cases} \tag{20}$$

When a constant magnet thickness is desirable to use for all flux-barrier layers, $\gamma_{dm2}$ and $\gamma_{dm3}$ can be set equal to 1 during the optimization. $dm_1$ is a dependent variable, and its value is equal:

$$dm_1 = wry \times \frac{K_{\text{air}}}{1 - K_{\text{air}}} \times \frac{1}{(1 + \gamma_{dm2} + \gamma_{dm2}\gamma_{dm3})} \tag{21}$$

Equation (14) shows the constraints on the width of magnets. The maximum allowable width for a magnet in barrier 1 is shown in Figure 3, and it is equal to:

$$wm_{1,\max} = 2\left(\frac{D_{\text{sh}}}{2} + wry_1\right)\tan\left(\frac{\alpha_p}{2}\right) \tag{22}$$

The following per-unit variables are defined for the width of magnets:

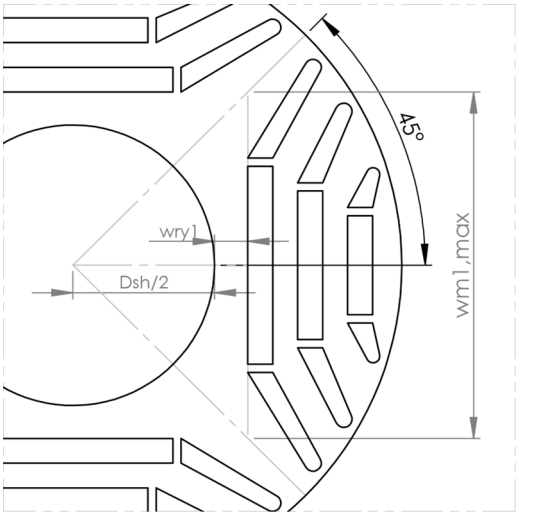


**Figure 3.**
Maximum value for $wm_1$

$$\begin{cases} \gamma_{wm1} = \dfrac{wm_1}{wm_{1,\max}} \leq 1 \\ \gamma_{wm2} = \dfrac{wm_2}{wm_1} \leq 1 \\ \gamma_{wm3} = \dfrac{wm_3}{wm_2} \leq 1 \end{cases} \tag{23}$$

The constraints on barrier arc angles are shown in equation (15). According to the flux lines pattern for the solid rotor, the angle of each barrier is higher than half of the rotor pole pitch-angle. Therefore,

$$\begin{cases} \gamma_{ba1} = \dfrac{ba_1}{\alpha_p/2} \geq 1 \\ \gamma_{ba2} = \dfrac{ba_2}{ba_1} \geq 1 \\ \gamma_{ba3} = \dfrac{ba_3}{ba_2} \geq 1 \end{cases} \tag{24}$$

According to the flux lines pattern for the solid rotor, it can be seen that the width of the flux tubes reduces as they approach the rotor surface. Therefore, the thickness of a flux barrier should reduce when it approaches the rotor surface. The maximum diameter for the barrier end circle 1 is shown in Figure 4, and it is equal to:

$$dbec_{1,\max} = dm_1 \times \sin(ba_1) \tag{25}$$

per-unit variables for the diameter of barrier end circles are defined as follows:

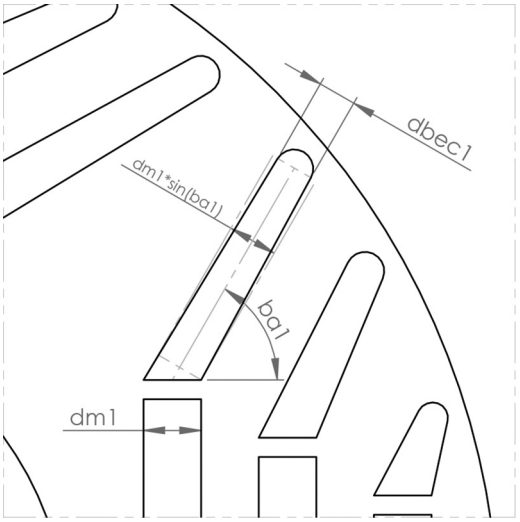


**Figure 4.**
Maximum value for diameter of a barrier end circle

$$\begin{cases} \gamma_{dbec1} = \dfrac{dbec_1}{dbec_{1,\max}} \le 1 \\ \gamma_{dbec2} = \dfrac{dbec_2}{dbec_{2,\max}} \le 1 \\ \gamma_{dbec3} = \dfrac{dbec_3}{dbec_{3,\max}} \le 1 \end{cases} \tag{26}$$

The per-unit rotor model is summarized into the following decision variables vector:

$$\begin{aligned} x = [&K_{\text{air}}, wry, wtrib, wrrib_1, wrrib_2, wrrib_3, \\ &\gamma_{wry2}, \gamma_{wry3}, \gamma_{wry4}, \gamma_{dm2}, \\ &\gamma_{dm3}, \gamma_{wm1}, \gamma_{wm2}, \gamma_{wm3}, \gamma_{ba1}, \gamma_{ba2}, \\ &\gamma_{ba3}, \gamma_{dbec1}, \gamma_{dbec2}, \gamma_{dbec3}] \end{aligned} \tag{27}$$

## 3. Proposed optimization method

Because the average electric torque in a SynRM is proportional to the magnetic saliency ratio of the rotor, the main objective in the rotor shape optimization is the maximization of the saliency ratio Oprea *et al.* (2015`). We should pay special attention to holding the torque ripple as low as possible when maximizing the saliency ratio.

Figure 5 shows the flowchart of the proposed method. In this method, the variables with the same geometrical properties are collected into individual groups, and the optimization is done on each group sequentially. According to equation (27), the number of independent decision variables for the rotor geometry is 20. Four of them are the width of the tangential and radial ribs, and their values should be considered based on the mechanical constraints of the rotor lamination. The values of these four variables are fixed during the optimization process. Therefore, the decision variables vector in the optimization is as follows:

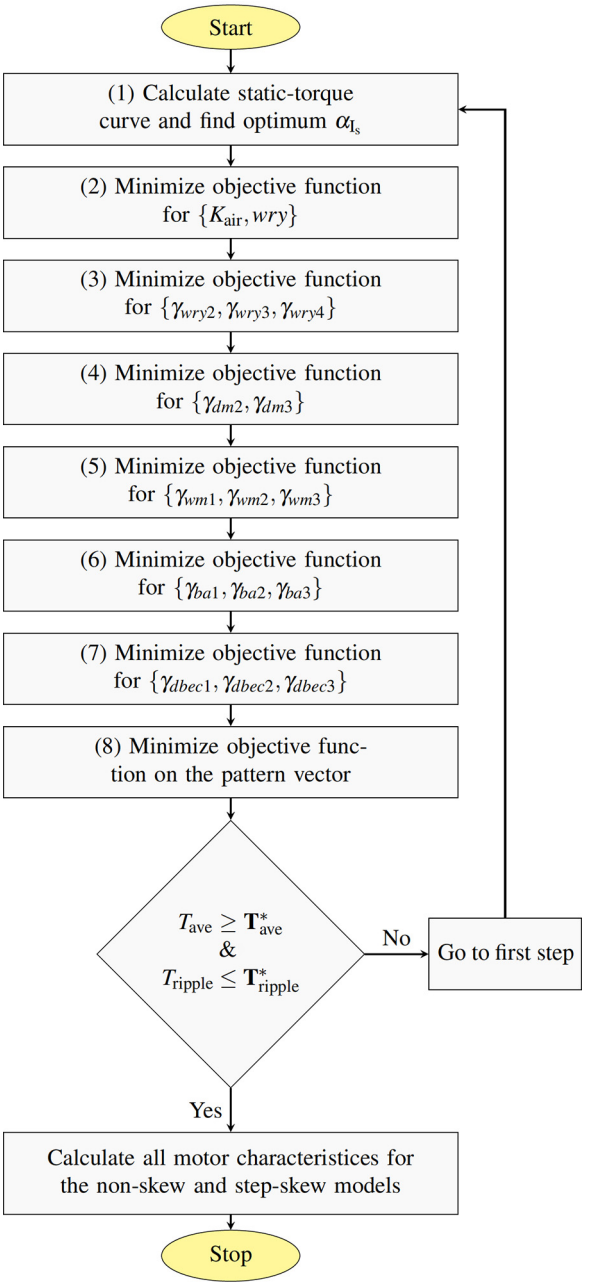


**Figure 5.**
Proposed method for rotor shape optimization

$$x = [K_{\text{air}}, wry, \gamma_{wry2}, \gamma_{wry3}, \gamma_{wry4}, \gamma_{dm2}, \gamma_{dm3}, \gamma_{wm1}, \gamma_{wm2}, \gamma_{wm3}, \gamma_{ba1}, \gamma_{ba2}, \gamma_{ba3}, \gamma_{dbec1}, \gamma_{dbec2}, \gamma_{dbec3}] \tag{28}$$

In this work, we used MATLAB software to implement the optimization algorithm, and we used the ANSYS Maxwell software for the FEA of the design samples.

The first step in the forward search path of the presented method is finding the optimum value for the stator current angle. This optimum number is calculated with the aim of the static-torque curve. In the next steps, the calculation of the electrical torque waveform under steady-state conditions is based on this optimum stator current angle.

The method of Hooke and Jeeves is used for the optimization. This method performs two types of search: exploratory search and pattern search Bazaraa *et al.* (2013). Exploratory search is done in Steps 2–7, and pattern search is done in Step 8 of the forward search path. The design variable is scaled-down and scaled-up by a factor $\alpha$ to find a neighbor minimum in each exploratory search. The value of the scale factor is a number greater than 1.

Different objective functions could be selected for the minimization, such as:

$$\begin{aligned} f_1 &= \frac{T_{\text{e,max}} - T_{\text{e,min}}}{T_{\text{ave}}} \\ f_2 &= -T_{\text{ave}} \\ f_3 &= \max\left\{ \left| \frac{T_{\text{ave}} - T_{\text{ave,d}}}{T_{\text{ave,d}}} \right|, \frac{T_{\text{e,max}} - T_{\text{e,min}}}{T_{\text{ave}}} \right\} \end{aligned} \tag{29}$$

$f_1$ in equation (29) denotes the torque ripple. This objective function is selected when a low torque ripple value is desirable. $f_2$ is used when the goal is to maximize the average torque. When we are trying to minimize the torque ripple and maximize the average torque simultaneously, a combination of $f_1$ and $f_2$ should be used. $f_3$ is one example. In $f_3$, $T_{\text{ave,d}}$ is the desired average torque. The value of this torque in our case is 4.8 Nm. $f_3$ could be used when we are trying to get the desired average torque with a minimum torque ripple.

The following sample code shows the implementation of the exploratory search for minimization of the torque ripple in Steps 2–7 in the MATLAB software [objective function is $f_1$ in equation (29)]

```
for i = 1:lentgh(x)
  x(i) = max(x(i) / alpha, x_min(i));
  CalculateTeByFEA();

  if (Tripple_new > Tripple_old)
     resetOldValues();
     x(i) = min(alpha^2 * x(i), x_max(i));
     CalculateTeByFEA();

     if (Tripple_new > Tripple_old)
        resetOldValues();
        x(i) = x(i) / alpha;
        fail_vector(i) = true;

     end
  end
end
```

In the first line of the for-loop, the value of $i$th design variable is reduced by dividing it by $\alpha$, and the resultant is limited from the low side by the corresponding minimum value. Then, the torque waveform is calculated by the FEA. In the case of further torque ripple reduction, we optimize the next design variable in the for-loop. Otherwise, the value of $i$th design variable increases by multiplying it by $\alpha_2$, and the resultant is limited from the high side by the corresponding maximum value. Again, the torque waveform is calculated by the FEA. If we do not get a new minimum value, we are already at a minimum point for this design variable, and the value of $i$th component of the fail vector should be set as true. After doing an exploratory search for all design variables, the pattern search is done in Step 8. Design variable vectors after Step number 7 in each iteration are stored and used to calculate the pattern vector. The pattern vector for the pattern search in the $i$th iteration is as follows:

$$v^i_{\text{pattern}} = x^i_7 - x^{i-1}_7 \tag{30}$$

Two conditions should be checked after each forward search path to terminate the optimization process. The first condition checks if the average torque $T_{\text{ave}}$ is greater than the desired average output torque $\mathbf{T}^*_{\mathbf{ave}}$. The second condition checks if the torque ripple $T_{\text{ripple}}$ is lower than the desired torque ripple $\mathbf{T}^*_{\mathbf{ripple}}$. When these two conditions are true, the optimization process will terminate, and all motor characteristics will be calculated and reported for both the nonskew and rotor step-skew models.

## 4. Results and discussion

In this paper, a 0.75 kW-1,500 rpm PMaSynRM is considered. The grade of the electrical steel in the stator and the rotor core is M470-50A, and the magnets are ferrite with grade Y30BH. The stator core was designed like the one in an IM. The number of poles is 4, and the number of the stator slots is 36. The stator winding is double-layer, and the coil span is equal to 8.

### *4.1 Convergence analysis*

The objective function $f_1$ in equation (29) is considered to analyze the convergence property of the proposed method. The aim of the objective function $f_1$ is the minimization of the torque ripple. To start the optimization process, a good initial decision variables vector should be considered. Because the rotor geometry model is a per-unit model, indicating a good starting value is not a complex task. The following vector is considered as the initial decision variables vector:

$$x^0 = [0.44, 11.5\text{mm}, 1, 1, 1, 1, 1, 0.7, 0.7, 0.7, 1, 1, 1, 1, 1, 1] \tag{31}$$

We should consider a proper maximum value and minimum value for each of the design variables based on equations in Section 2.1 to confirm all design samples exist in a feasible region. The minimum decision variables vector is as in the following:

$$x_{\min} = [0.3, 9.5\text{mm}, 0.8, 0.8, 0.8, 0.7, 0.7, 0.4, 0.4, 0.4, 1, 1, 1, 0.5, 0.5, 0.5] \tag{32}$$

And the maximum one is as follows:

$$x_{\max} = [0.6, 13.5\text{mm}, 1, 1, 1, 1, 1, 0.8, 0.8, 0.8, 1.2, 1.4, 1.6, 1, 1, 1] \tag{33}$$

The value of scale factor $\alpha$ considered in this optimization is 1.025. Figure 6 shows the average output torque vs iteration number. Figure 7 shows the torque ripple vs iteration number. As you can see, the value of the torque ripple for the first sample is around 25%, and for the final sample is below 7%. The algorithm is convergent; however, there are some spikes during the optimization.

Figure 8 shows all the investigated design samples during the optimization on the $T_{ave}$-$T_{ripple}$ plane. As can be seen, after iteration number 40, most samples are close to each other.

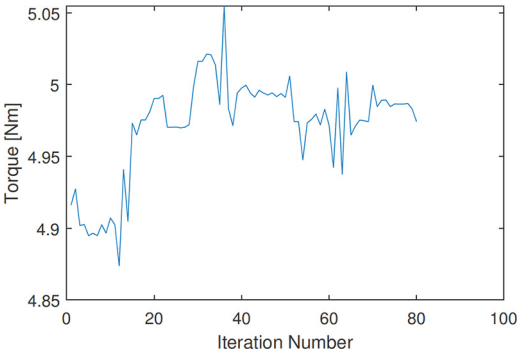


**Figure 6.**
The average torque vs the iteration number in the convergence analysis

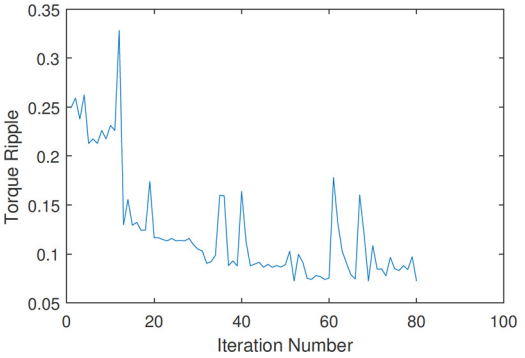


**Figure 7.**
The torque ripple vs the iteration number in the convergence analysis

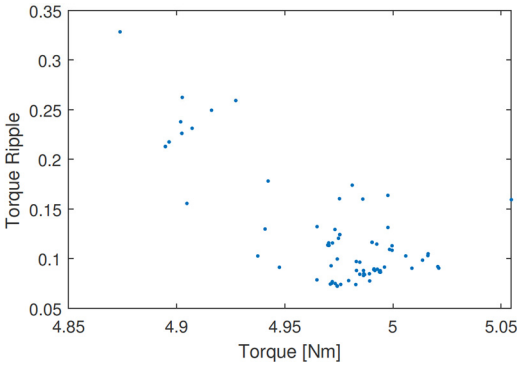


**Figure 8.**
All design samples in the $T_{ave}$-$T_{ripple}$ plane in the convergence analysis

Figure 9 represents the electrical torque as a function of time for the initial and final design samples. The amount of the torque ripple for the final sample is lower than one-third of the value of the torque ripple for the initial case. Because of considering a proper $x^0$, the average torque of the initial case is close to the rated motor torque. Therefore, selecting the minimum torque as an optimization objective works well for this case.

Figure 10 shows the static-torque curve for the initial and final samples. The maximum torque value for the final sample is greater than the initial sample.

Figure 11 shows the rotor sketch of the final design sample after optimization. The optimum decision variables vector is as follows:

$$x^* = [0.46228, 11.5\text{mm}, 0.95181, 0.95181, 0.9286, 1, 1, 0.7175, 0.7175, 0.75382,$$
$$1.025, 1, 1.0769, 0.95181, 1, 0.95181] \tag{34}$$

Figure 12 represents the magnetic field distribution of the initial and final design samples in the convergence analysis.

*4.2 Analysis of different operating points*

It should be noted that the calculations of the torque ripple and the average torque for design samples during the optimization were done for a single operating point.

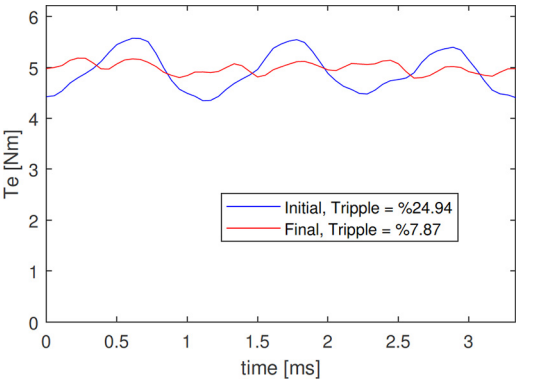


**Figure 9.**
The electrical torque vs time for the initial and final design samples in the convergence analysis

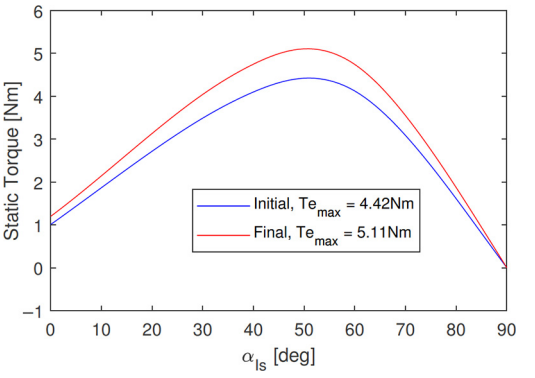


**Figure 10.**
The static-torque curve for the initial and final design samples in the convergence analysis

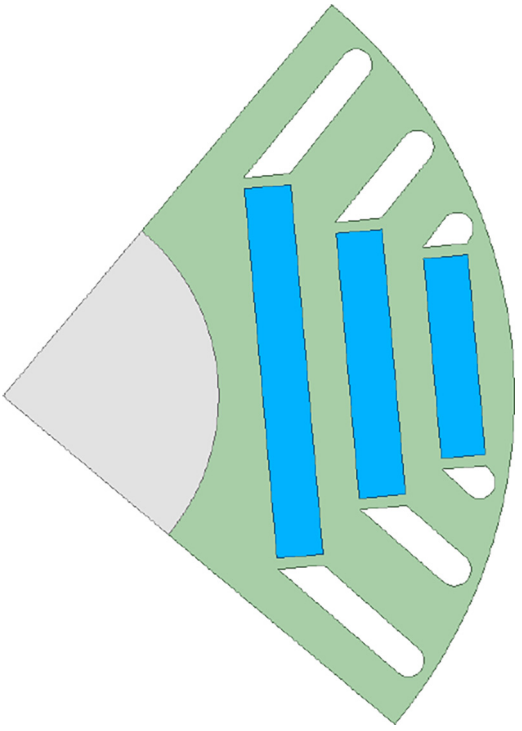

**Figure 11.**
The rotor sketch of the optimum design sample considering the minimum torque ripple as objective function, the depth of magnets is considered the same

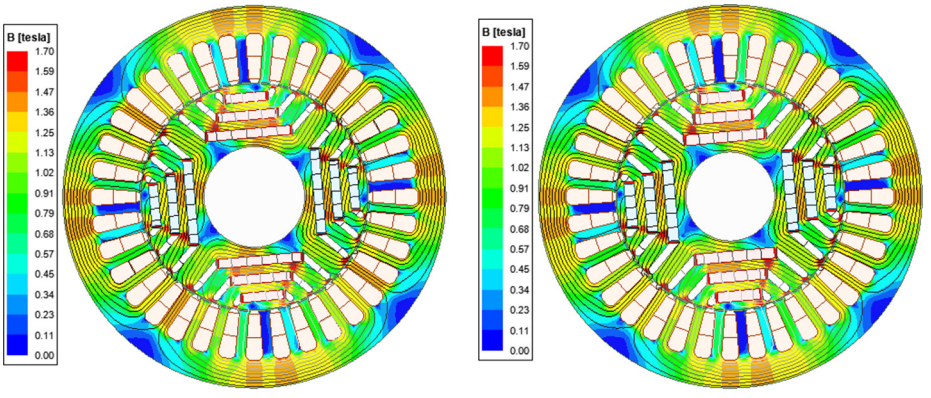


**(a)** **(b)**

**Notes:** (a) Initial design; (b) final design

**Figure 12.**
The magnetic field distribution of the initial and final design samples in the convergence analysis

However, the value of the torque ripple should be within a reasonable range for other operating points.

Several simulations were done to analyze the effect of the stator current amplitude and angle on the torque ripple and the average torque. Figure 13 shows electrical torque as a

function of time for different stator current excitation levels and angles. According to the figure, the torque ripple increases when the current excitation level decreases. For each excitation current level, the variation of the torque ripple is low when $\alpha_{I_s}$ it changes from 45° to 55°.

*4.3 Step-skew study*

Several steady-state simulations were done on the step-skew model to investigate the effect of skewing on further torque ripple reduction. Figure 14 shows the electrical torque as a function of time for the step-skew model. The torque ripple in this operating range for the step-skew model is around 2%. Table 1 presents the summary of the results. The skew angle is equal to one stator slot pitch angle, which is 10°. The motor stack length is 70 mm, and the number of steps considered in the step-skew rotor model is 7. According to the table, step-skew can effectively reduce the torque ripple value.

*4.4 Robustness analysis*

Robustness means that the algorithm should converge when we start with different initial decision variable vectors. The optimization was done considering the following inappropriate initial decision variables vector to investigate the robustness of the proposed method,

$$x^0 = [0.44, 11.5\text{mm}, 0.8, 0.8, 0.8, 1, 1, 0.5, 0.5, 0.5, 1.1, 1.1, 1.1, 0.8, 0.6, 0.7] \quad (35)$$

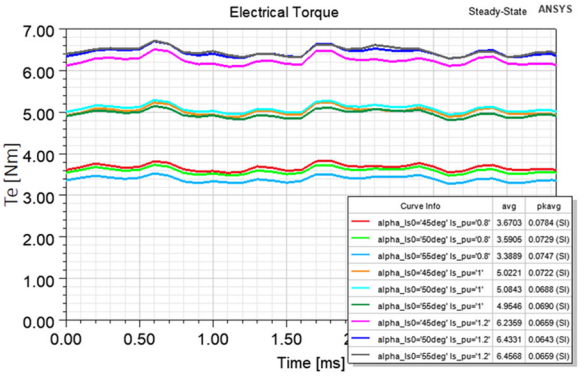


**Figure 13.**
The electrical torque vs time for different stator current levels and angles for the nonskew model in the convergence analysis

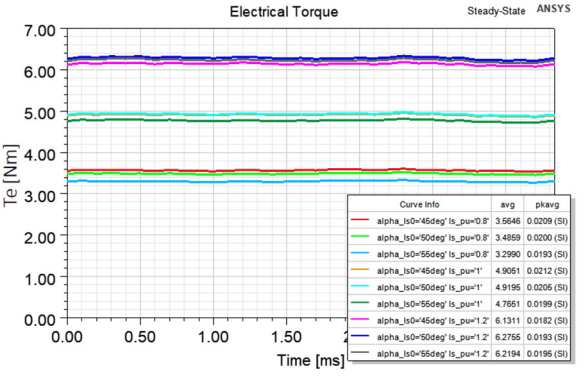


**Figure 14.**
The electrical torque vs time for different stator current levels and angles for the step-skew model in the convergence analysis

Figure 15 shows the initial rotor geometry for robustness analysis. The initial decision variables vector is not acceptable because the value of its average torque is low in comparison with the desired rated torque (the value of rated torque is 4.8 Nm). A mixed objective function is considered in this case. At first, the objective function is the maximization of the average torque. When the desired average torque is achieved, the objective function will be switched to minimize the torque ripple. Figure 16 shows the value of the average output torque vs the iteration number. The desired average torque is achieved at iteration Number 75. After this iteration number, the objective function switches to the minimum torque ripple.

| $I_{s,pu}$ | $\alpha_{I_s}$ [deg] | Average torque (Nm) | | Torque ripple % | |
|---|---|---|---|---|---|
| | | Nonskew | Skew | Nonskew | Skew |
| 0.8 | 45 | 3.67 | 3.56 | 7.84 | 2.09 |
| 0.8 | 50 | 3.59 | 3.49 | 7.29 | 2.00 |
| 0.8 | 55 | 3.39 | 3.29 | 7.47 | 1.93 |
| 1 | 45 | 5.02 | 4.91 | 7.22 | 2.12 |
| 1 | 50 | 5.08 | 4.92 | 6.88 | 2.05 |
| 1 | 55 | 4.95 | 4.77 | 6.90 | 1.99 |
| 1.2 | 45 | 6.24 | 6.13 | 6.59 | 1.82 |
| 1.2 | 50 | 6.43 | 6.27 | 6.43 | 1.93 |
| 1.2 | 55 | 6.45 | 6.22 | 6.59 | 1.95 |

**Table 1.** The average torque and torque ripple for the nonskew and step-skew models of the optimal design in the convergence analysis

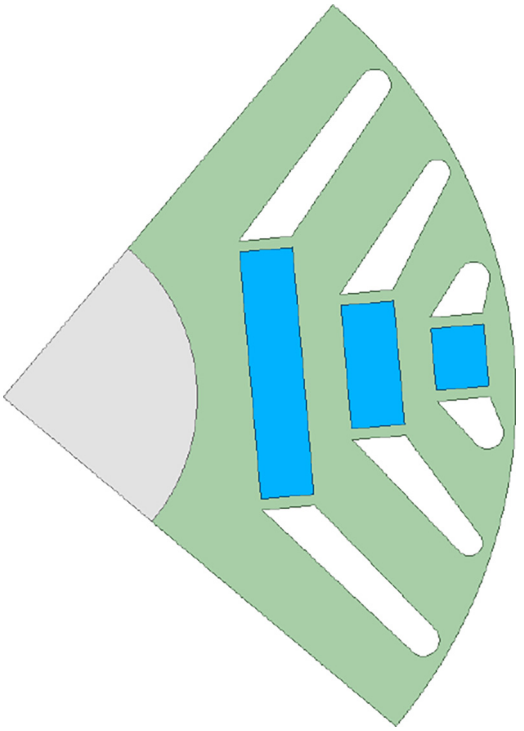

**Figure 15.** The initial rotor sketch in the robustness analysis, size of magnets and barrier angles are considered inappropriate

The torque ripple vs the iteration number is shown in Figure 17. As you can see, before iteration Number 75, there is no considerable reduction in the torque ripple during the average torque maximization. After iteration Number 75, the optimization solver tries to minimize the torque ripple. The torque ripple is reduced from 60% to 10%. Variation of the average torque is negligible during the minimization of the torque ripple. According to the results, we can maximize the average torque and minimize the torque sequentially until reaching the desired values.

Figure 18 shows all the investigated design samples during optimization on the $T_{ave}$ -$T_{ripple}$ plane. The switch in the objective function is obvious. Along Path (1), the solver tries to maximize the average torque. Path (2) shows the direction of minimizing the torque ripple. During Path (1), the scale factor $\alpha$ is equal to 1.1, and for Path (2), $\alpha$ is equal to 1.05.

Figure 19 shows the electrical torque as a function of time for the initial and final design samples. The average torque is low for the initial design sample, and the torque ripple is high. The average torque is improved in the final design sample, and the torque ripple is reduced. Figure 20 shows the static-torque curve for the initial and final design samples. The maximum torque is increased from 3.14 Nm to 4.72 Nm.

Figure 21 shows the optimum rotor sketch. The optimum decision variables vector is as follows:

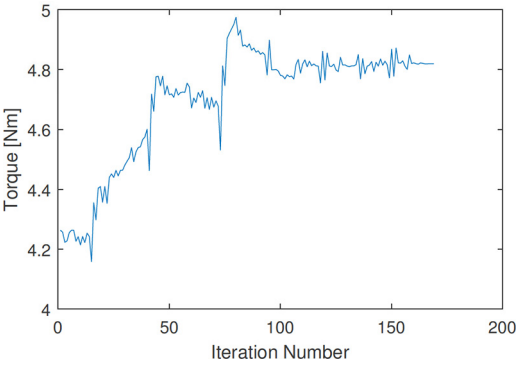


**Figure 16.**
The average torque vs the iteration number for initial and final design samples in the robustness analysis

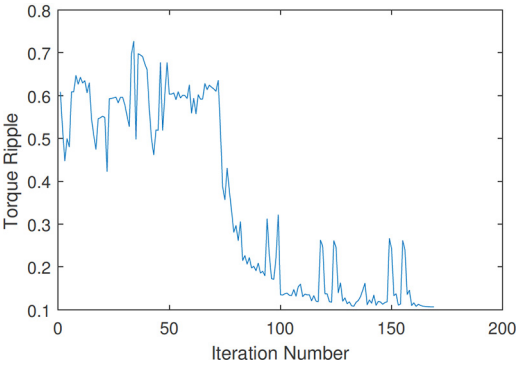


**Figure 17.**
The torque ripple vs the iteration number for initial and final design samples in the robustness analysis

$$x^* = [0.45455, 12.075\text{mm}, 0.9064, 0.9434, 0.94637, 0.88109, 0.79913, 0.70603, 0.67241, 0.441, 1.0476, 1.05, 1.05, 0.81566, 0.6798, 0.59046] \quad (36)$$

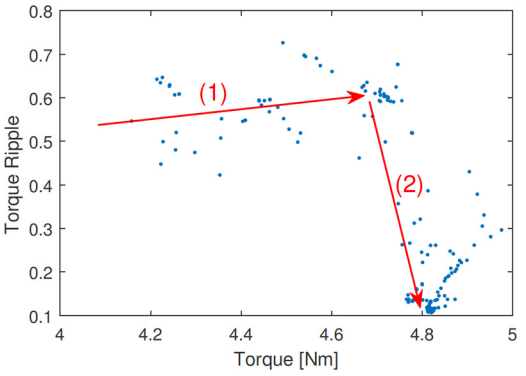


**Figure 18.** All design samples in the $T_{ave}$ - $T_{ripple}$ plane in the robustness analysis, as you can see, even starting with an inappropriate initial decision variables vector, the algorithm can converge to a desirable design

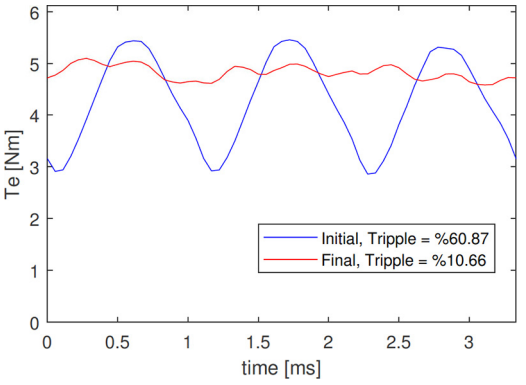


**Figure 19.** The electrical torque for the initial and final design samples in the robustness analysis

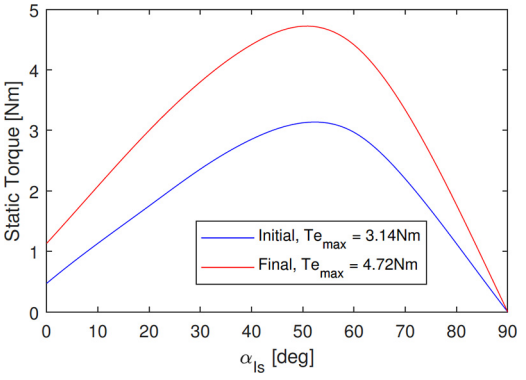


**Figure 20.** The static-torque curve for the initial and final design samples in the robustness analysis

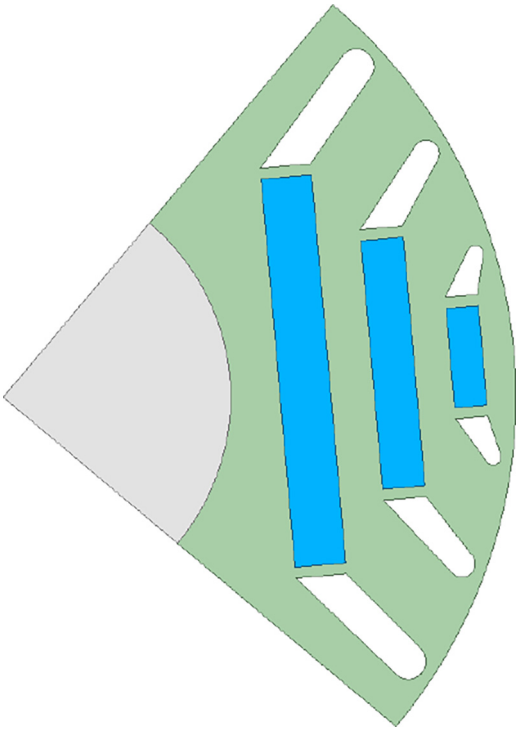

**Figure 21.**
The optimum rotor sketch in the robustness analysis

Like the previous case, several steady-state simulations were done to analyze the effect of stator current amplitude and angle on the torque ripple and the average torque. Figures 22 and 23 show the results for the nonskew and the step-skew model in the robustness analysis cases, respectively. Summary of the results are reported in Table 2. The torque ripple for the nonskew model in the reported operating range is around 10%, whereas the torque ripple for the step-skew model is lower than 3%. Figure 24 represents the magnetic field distribution of the initial and final design samples in the robustness analysis. As you can see, we have saturation in some of the stator teeth in the initial design, but in the final design, the flux density variation in the stator teeth is more sinusoidal.

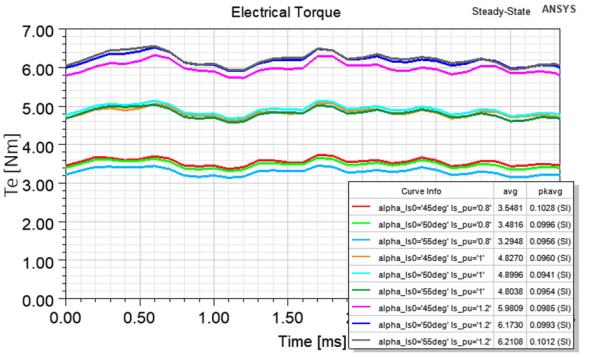


**Figure 22.**
The electrical torque vs time for different stator current levels and angles for the nonskew model of the optimal design in the robustness analysis

## 5. Conclusion

A sequential iterative method was presented based on the per-unit rotor model for rotor shape optimization in SynRMs. The performance of the proposed method was studied on a three-phase 0.75 kW-1,500 rpm PM assisted SynRMs. Different cases such as nonskew and step-skew rotor models were investigated, and convergence and robustness of the method

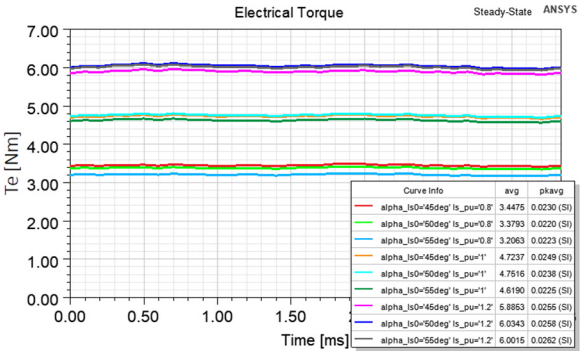


**Figure 23.**
The electrical torque vs time for different stator current levels and angles for the step-skew model of the optimal design in the robustness analysis

| $I_{s,pu}$ | $\alpha_{I_s}$ [deg] | Average torque (Nm) | | Torque ripple % | |
|---|---|---|---|---|---|
| | | Nonskew | Skew | Nonskew | Skew |
| 0.8 | 45 | 3.55 | 3.45 | 10.28 | 2.30 |
| 0.8 | 50 | 3.48 | 3.38 | 9.96 | 2.20 |
| 0.8 | 55 | 3.29 | 3.21 | 9.56 | 2.23 |
| 1 | 45 | 4.83 | 4.72 | 9.60 | 2.49 |
| 1 | 50 | 4.90 | 4.75 | 9.41 | 2.38 |
| 1 | 55 | 4.80 | 4.62 | 9.54 | 2.25 |
| 1.2 | 45 | 5.98 | 5.88 | 9.85 | 2.55 |
| 1.2 | 50 | 6.17 | 6.03 | 9.93 | 2.58 |
| 1.2 | 55 | 6.21 | 6.00 | 10.12 | 2.62 |

**Table 2.**
The average torque and torque ripple for the nonskew and step-skew models of the optimal design in the robustness analysis

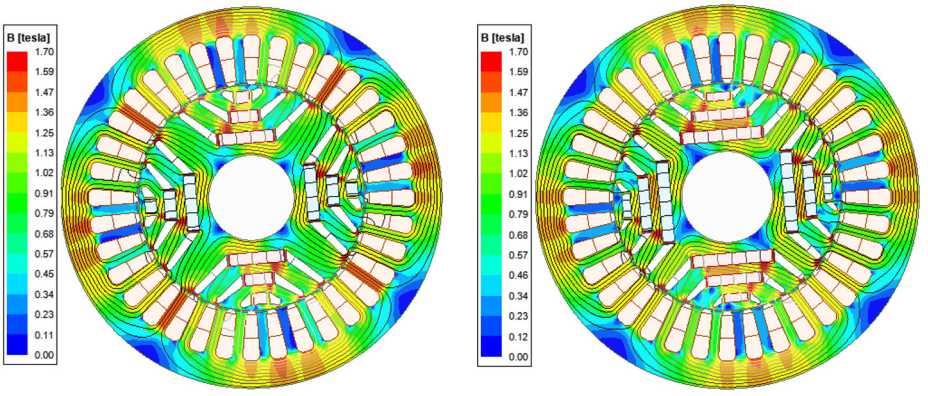


**(a)** **(b)**

**Notes:** (a) Initial design; (b) final design

**Figure 24.**
The magnetic field distribution of the initial and final design samples in the robustness analysis

were analyzed. It was shown that the method is robust enough and can converge within an acceptable number of iterations. The per-unit rotor model was introduced to make optimization and geometrical calculations easier. One benefit of working with the per-unit rotor model is scaling. When optimization is done for a specific motor rating, it can be scaled up or down for other ratings with little effort.

## References

Babetto, C., Bacco, G. and Bianchi, N. (2018), "Synchronous reluctance machine optimization for high-speed applications", *IEEE Transactions on Energy Conversion*, Vol. 33 No. 3, pp. 1266-1273.

Bacco, G. and Bianchi, N. (2019), "Design criteria of flux-barriers in synchronous reluctance machines", *IEEE Transactions on Industry Applications*, Vol. 55 No. 3, pp. 2490-2498.

Baka, S., Sashidhar, S. and Fernandes, B.G. (2021), "Design of an energy efficient line-start two-pole ferrite assisted synchronous reluctance motor for water pumps", *IEEE Transactions on Energy Conversion*, Vol. 36 No. 2, pp. 961-970.

Bazaraa, M.S., Sherali, H.D. and Shetty, C.M. (2013), *Nonlinear Programming: Theory and Algorithms*, John Wiley and Sons.

Bianchi, N., Bolognani, S., Bon, D. and PrÉ, M.D. (2008), "Torque harmonic compensation in a synchronous reluctance motor", *IEEE Transactions on Energy Conversion*, Vol. 23 No. 2, pp. 466-473.

Cai, H., Guan, B., Xu, L. and Choi, W. (2014), "Optimal design of synchronous reluctance machine", *COMPEL: The International Journal for Computation and Mathematics in Electrical and Electronic Engineering*, Vol. 33 No. 5, pp. 1569-1586, doi: 10.1108/COMPEL-09-2013-0287.

Choi, Y.C., Kim, H.-S. and Lee, J.-H. (2008), "Optimum design criteria for maximum torque density and minimum torque ripple of synrm according to the rated wattage using response surface methodology", *IEEE Transactions on Magnetics*, Vol. 44 No. 11, pp. 4135-4138.

Cupertino, F., Pellegrino, G. and Gerada, C. (2014), "Design of synchronous reluctance motors with multiobjective optimization algorithms", *IEEE Transactions on Industry Applications*, Vol. 50 No. 6, pp. 3617-3627.

Guan, Y., Zhu, Z.Q., Afinowi, I.A.A., Mipo, J.C. and Farah, P. (2016), "Design of synchronous reluctance and permanent magnet synchronous reluctance machines for electric vehicle application", *COMPEL: The International Journal for Computation and Mathematics in Electrical and Electronic Engineering*, Vol. 35 No. 2, pp. 586-606, doi: 10.1108/COMPEL-02-2015-0109.

Liu, H.-C., Seol, H.-S., Kim, J.-Y. and Lee, J. (2019), "Design and analysis of an ie4 class line-start synchronous reluctance motor considering total loss and starting performance", *Journal of Electronic Materials*, Vol. 48 No. 3, pp. 1386-1394.

Liu, X., Li, Y., Liu, Z., Ling, T. and Luo, Z. (2016), "Analysis and design of a high power density permanent magnet-assisted synchronous reluctance machine with low-cost ferrite magnets for evs/hevs", *COMPEL – The International Journal for Computation and Mathematics in Electrical and Electronic Engineering*, Vol. 35 No. 6, pp. 1949-1964, doi: 10.1108/COMPEL-05-2016-0233.

López-Torres, C., Garcia, A., Riba, J., Lux, G. and Romeral, L. (2018), "Computationally efficient design and optimization approach of pma-synrm in frequent operating torque–speed range", *IEEE Transactions on Energy Conversion*, Vol. 33 No. 4, pp. 1776-1786.

Mingardi, D. and Bianchi, N. (2017), "Line-start pm-assisted synchronous motor design, optimization, and tests", *IEEE Transactions on Industrial Electronics*, Vol. 64 No. 12, pp. 9739-9747.

Oprea, C., Dziechciarz, A. and Martis, C. (2015), "Comparative analysis of different synchronous reluctance motor topologies", *2015 IEEE 15th International Conference on Environment and Electrical Engineering (EEEIC)*, pp. 1904-1909, doi: 10.1109/EEEIC.2015.7165463.

Pellegrino, G., Jahns, T.M., Bianchi, N., Soong, W.L. and Cupertino, F. (2016), *The Rediscovery of Synchronous Reluctance and Ferrite Permanent Magnet Motors: tutorial Course Notes*, Springer.

Tarek, M.T.B. and Choi, S. (2017), "Design and rotor shape modification of a multiphase high speed permanent magnet assisted synchronous reluctance motor for stress reduction", *2017 IEEE Energy Conversion Congress and Exposition (ECCE)*, pp. 5389-5395, doi: 10.1109/ECCE.2017.8096902.

Wang, K., Zhu, Z.Q., Ombach, G., Koch, M., Zhang, S. and Xu, J. (2015), "Torque ripple reduction of synchronous reluctance machines", *COMPEL: The International Journal for Computation and Mathematics in Electrical and Electronic Engineering*, Vol. 34 No. 1, pp. 3-17, doi: 10.1108/COMPEL-11-2013-0366.

## Appendix

Detailed parameters of the PMaSynRM studied in this work are given in Table A1.

**Table A1.** Detailed parameters of the PMaSynRM studied in this paper

| Parameter | Value | Unit | Description |
|---|---|---|---|
| $P_{out}$ | 0.75 | kW | Output power |
| Speed | 1,500 | rpm | Rated speed |
| $V_t$ | 400 | V | Line voltage, root mean square (RMS) |
| $I_t$ | 1.65 | A | Full load phase current (RMS) |
| $N_s$ | 36 | – | Number of stator slots |
| $p$ | 4 | – | Number of poles |
| $OSD$ | 125 | mm | Outer stator diameter |
| $ISD$ | 75 | mm | Inner stator diameter |
| $L_{stk}$ | 70 | mm | Stack length |
| $g$ | 0.5 | mm | Air gap length |
| $D_{sh}$ | 32 | mm | Shaft diameter |
| $N_{layers}$ | 2 | – | Number of winding layers |
| Span | 8 | Slots | Number of slots between two coil arms |
| $N_{tc}$ | 50 | Turns | Number of turns per coil |
| $N_p$ | 1 | – | Number of parallel paths |
| $R_{ph}$ | 14.3 | Ω | Hot phase resistance |

**Corresponding author**
Ali Jamali Fard can be contacted at: a.jamalifard@aut.ac.ir

For instructions on how to order reprints of this article, please visit our website:
**www.emeraldgrouppublishing.com/licensing/reprints.htm**
Or contact us for further details: **permissions@emeraldinsight.com**